Front. Optoelectron. 2019, 12(1): 69–87
https://doi.org/10.1007/s12200-017-0743-3

REVIEW ARTICLE

Modulation of orbital angular momentum on the propagation dynamics of light fields

Peng LI (✉), Sheng LIU, Yi ZHANG, Lei HAN, Dongjing WU, Huachao CHENG, Shuxia QI, Xuyue GUO, Jianlin ZHAO

MOE Key Laboratory of Material Physics and Chemistry under Extraordinary Conditions, and Shaanxi Key Laboratory of Optical Information Technology, School of Science, Northwestern Polytechnical University, Xi'an 710072, China

Abstract Optical vortices carrying orbital angular momentum (OAM) have attracted extensive attention in recent decades because of their interesting applications in optical trapping, optical machining, optical communication, quantum information, and optical microscopy. Intriguing effects induced by OAMs, such as angular momentum conversion, spin Hall effect of light (SHEL), and spin–orbital interaction, have also gained increasing interest. In this article, we provide an overview of the modulations of OAMs on the propagation dynamics of scalar and vector fields in free space. First, we introduce the evolution of canonical and noncanonical optical vortices and analyze the modulations by means of local spatial frequency. Second, we review the Pancharatnam–Berry (PB) phases arising from spin–orbital interaction and reveal the control of beam evolution referring to novel behavior such as spin-dependent splitting and polarization singularity conversion. Finally, we discuss the propagation and focusing properties of azimuthally broken vector vortex beams.

Keywords orbital angular momentum, polarization, spin angular momentum, Pancharatnam–Berry (PB) phase, angular diffraction

1 Introduction

Scientists have realized that light fields carry linear and angular momenta after the pioneering work of Poynting [1]. The angular momentum carried by a light field can be divided into the spin and orbital parts [2,3], which are conventionally associated with a circular polarization state and vortex phase, respectively. The spin angular momentum (SAM) is an intrinsic property of photons, similar to the SAM of electrons; it has quantitated values of $\pm\hbar$ and depends on the circular polarization state of the light field. The orbital angular momentum (OAM), however, can be further divided into intrinsic and extrinsic OAMs [2]. In 1992, Allen et al. recognized that light fields with spiral phases carry intrinsic OAMs [4]. This intrinsic OAM carried by each photon can be many times greater than the SAM [2,4]. Immediately after the detection reported by Woerdman [5–7], several studies in this new area of light physics began. Meanwhile, light beams carrying intrinsic OAMs have found practical applications in optical trapping, optical machining, optical communication, quantum information, optical microscopy, and so on [8–10]. Extrinsic OAMs arise from the cross product of the total linear momentum transported by the beam and position of its axis relative to the origin of coordinates [2]. Therefore, the total angular momentum of a light field can be presented in the form of three summands.

Simultaneously, particular interest was paid to the interaction of angular momenta, which produce nontrivial evolution of light fields [11–16]. The interaction between SAMs and extrinsic OAMs leads to the transverse deflection of circularly polarized beams when propagating in inhomogeneous media, including the polarization-dependent Imbert–Fedorov effect of a light beam reflected or refracted at the interface between two media and splitting of rays in inhomogeneous anisotropic media [13,17–20]. The interaction between intrinsic and extrinsic OAMs leads to significantly enhanced transverse deflection with respect to the values for the topological charge of the vortex phase [17,21,22], similar to the Magnus effect of light [23]. In this article, we review the modulations of OAMs on the propagation dynamics of light fields, considering both scalar and vector fields. In Section 2, we introduce the basic theoretical description of OAM for generic light fields. In Section 3, we describe the evolutions of canonical and noncanonical optical vortices

Received August 7, 2017; accepted September 27, 2017

E-mail: pengli@nwpu.edu.cn

and emphatically analyze the modulation based on local spatial frequency. In Section 4, we present the Pancharatnam–Berry (PB) phases that stem from spin–orbital interaction and discuss the novel propagation dynamics induced by spatially variant PB phases. Finally, we give an overview on the propagation and focusing properties of azimuthally broken vector vortex beams.

2 OAM of light fields

First, we consider a monochromatic plane wave propagating along the z-axis in free space, of which the electric and magnetic components are characterized as $\boldsymbol{E}$ and $\boldsymbol{B}$, respectively. Considering the time-harmonic feature of a light filed, the time-averaged linear momentum density can be expressed as

$$\boldsymbol{p} = \frac{\varepsilon_0}{2}\mathrm{Re}(\boldsymbol{E}^* \times \boldsymbol{B}). \tag{1}$$

A uniformly polarized paraxial light field has vector potential denoted as $\boldsymbol{A} = u(x,y,z)\exp[-\mathrm{i}(\omega t - kz)](\boldsymbol{e}_x + \mathrm{i}\sigma\boldsymbol{e}_y)$, where $u(x,y,z)$ is the normalized complex amplitude, ω is the frequency, $k = \omega/c$ is the wavenumber, $\boldsymbol{e}_x$ and $\boldsymbol{e}_y$ are the unit vectors, $\sigma = \mathrm{i}(\alpha\beta^* - \alpha^*\beta)$ is the polarization ellipticity, and α and β are the complex amplitude of two orthogonal polarizations with $|\alpha|^2 + |\beta|^2 = 1$. The time-averaged linear momentum density thus can be rewritten in the cylindrical coordinate system as

$$\boldsymbol{p} = \frac{\mathrm{i}\varepsilon_0\omega}{2}(u^*\nabla u - u\nabla u^*) + \varepsilon_0\omega k|u|^2\boldsymbol{e}_z + \frac{\varepsilon_0\omega\sigma}{2}\frac{\partial|u|^2}{\partial r}\boldsymbol{e}_\phi, \tag{2}$$

where $\boldsymbol{e}_z$ and $\boldsymbol{e}_\phi$ are the longitudinal and azimuthal unit vectors in the cylindrical coordinate system, respectively. Thus, the total angular momentum can be obtained by integrating the cross product of linear momentum density with the radius vector $\boldsymbol{r} = (r,0,z)$ — i.e., $\boldsymbol{J} = \varepsilon_0(\boldsymbol{r} \times \boldsymbol{p})\mathrm{d}\boldsymbol{r}$ [24]. From Eq. (2), we can find that, when $\sigma = 0$ — that is, for the linearly polarized plane waves — there cannot be any component of angular momentum, whereas for the circularly polarized plane waves — i.e., $\sigma \neq 0$ — there are pure SAMs with respective to the spin state σ.

Nevertheless, Allen et al. noted that, for the Laguerre–Gaussian (LG) mode with complex amplitude [6,25]

$$\begin{aligned}\mathrm{LG}_{l,p}(r,\phi) = &\sqrt{\frac{2p!}{\pi(p+|l|)!}}\frac{1}{w(z)}\left(\frac{\sqrt{2}r}{w(z)}\right)^{|l|} \\ &\times\exp\left(-\frac{r^2}{w(z)^2}\right)L_p^{|l|}\left[\frac{2r^2}{w(z)^2}\right] \\ &\times\exp(\mathrm{i}l\phi)\exp\left[-\mathrm{i}k\frac{r^2 z}{2(z_R^2+z^2)}\right]\exp[-\mathrm{i}\Phi],\end{aligned} \tag{3}$$

where $L_p^{|l|}$ is a normalized Laguerre polynomial with l and p denoting the azimuthal and radial variation of phase fronts, $z_R = kw_0^2/2$ is the Rayleigh range, $w(z) = w_0\sqrt{1+z^2/z_R^2}$ is the beam waist, $\Phi = (2p + |l| + 1)\tan^{-1}(z/z_R)$ corresponds to the Gouy phase, and (r,ϕ,z) are the cylindrical coordinates. The total angular momentum density can be described as [26]

$$\boldsymbol{j}_z = \left(\frac{l}{\omega}|u|^2 + \frac{\sigma r}{2\omega}\frac{\partial|u|^2}{\partial r}\right)\boldsymbol{e}_z. \tag{4}$$

Integrating this equation, we obtain the total angular momentum of $(l + \sigma)\hbar$ per photon. Obviously, the total angular momentum is divided into the orbital and spin parts with respect to the topological charge of the vortex phase and spin state, respectively.

For the generic fields, the linear momentum density can be deduced from the vector potential and can be given by [27]

$$\boldsymbol{p} = \frac{\varepsilon_0}{2\omega}\left\{\mathrm{Im}[\boldsymbol{E}^* \cdot (\nabla)\boldsymbol{E}] + \frac{1}{2}\nabla \times \mathrm{Im}[\boldsymbol{E}^* \times \boldsymbol{E}]\right\}. \tag{5}$$

These two terms in the right part of the above equation correspond to the orbital and spin parts of linear momentum. Particularly, the orbital part of linear momentum density is closely related to the local wave vector, depending on the phase gradient perpendicular to the wave vector. In consequence, the OAM caused by the gradient of the wave front is rewritten as

$$\boldsymbol{j}_o = \boldsymbol{r} \times \boldsymbol{p}_o = \frac{\varepsilon_0}{2\omega}\mathrm{Im}[\boldsymbol{E}^* \cdot (\boldsymbol{r} \times \nabla)\boldsymbol{E}]. \tag{6}$$

Integrating over the whole transverse field, one can obtain the OAM per photon.

The simplest example of a light field carrying OAMs is that with a canonical vortex phase in the transverse plane of $\exp(\mathrm{i}l\phi)$. Similar to classical mechanics, the OAM of a photon can exert forces and torques on both macroscopic and quantum objects [28–31]. It has been transferred from light fields to microsized particles and to atoms and Bose–Einstein condensates [2,8,32]. Moreover, the modes carrying distinct l are mutually orthogonal. Relying on this property, the OAMs have been regarded as another degree of freedom in optical and quantum communications [33–37]. Specifically, the OAM state is theoretically infinite, which makes the beams carrying OAMs appropriate candidates for developing the transmission capacity [38–41]. Furthermore, the OAM-based beams have promoted many other developments from optical microscopy to light processing and entanglement and quantum information [42–46]. However, these prospective applications are based on the investigation about the fundamental diffractive properties of beams carrying OAMs [47]. In other words, exploiting other OAM beams can further develop the practical applications [48–50].

3 Diffraction of fields carrying OAMs

3.1 Canonical vortices

As the scalar solution of Helmholtz equation in the cylindrical coordinate system, the LG eigenmodes were initially demonstrated carrying OAMs [4,51], and then recognized as the canonical vortices carrying OAMs. These beams have cylindrical symmetries of complex amplitude with an on-axis intensity null and vortex phase. Importantly, as described in Eq. (3), the LG beams are characterized by the parameters l and p. l is the azimuthal order giving an OAM of $l\hbar$ per photon — i.e., the so-called topological charge of vortex phase; p is the radial index denoting the ring number of intensity distribution. Figures 1(a)–1(d) show the intensity and phase distributions of four canonical vortices.

For LG beams, the OAMs are irrespective to the radial distribution of the beam. Hence, most attention was devoted to the LG beams with the zeroth radial index — namely, the $LG_{0,l}$ beams with a single-ringed profile. The evolution of $LG_{0,l}$ beams, as well as the focusing properties, were investigated immediately after the reported work of Allen, including on- and off-axis beams with different topological charges [52–54] and beams having single and multiple singularities [55–57]. The remarkable diffraction property of $LG_{0,l}$ beams is their divergence; that is, the $LG_{0,l}$ beams undergo obvious diffraction and rapid expansion of the hollow core with respect to the modulus of the topological charge — i.e., $|l|$. Moreover, the beam divergence angle increases with increasing OAM. Figure 1(e) displays the divergence of $LG_{0,l}$ beams generated from the transformation of a cylindrical lens (blue) and the forked diffraction grating (red), respectively. w_0 and r_{rms} correspond to the waist of Gaussian background and square root of the radial variance for the intensity distribution, respectively [58].

Recently, the LG beams with large radial index were reported with quasi-nondiffraction within the same propagation region as Bessel beams [59–62]. For the LG beams described in Eq. (2) with a large radial index, the amplitude terms can be approximately equivalent to the elegant Bessel function as [60]

$$\exp\left(-\frac{r^2}{w(z)^2}\right)\left(\frac{\sqrt{2}r}{w(z)}\right)^{|l|}L_p^{|l|}\left(\frac{2r^2}{w(z)^2}\right) \approx \frac{\Gamma(p+|l|+1)}{p!N^{|l|/2}}J_l\left(2\sqrt{2N}\frac{r}{w(z)}\right), \tag{7}$$

where $N = p + (|l| + 1)/2$, $\Gamma(\cdot)$ is the gamma function, and $J_l(\cdot)$ is the first type of Bessel function with order l. Figure 2 depicts the evolution behavior of a zeroth-order Bessel–Gauss beam as well as LG beams with $l = 1$, $p = 10$ and $l = 5$, $p = 10$. The Gauss background has the same waist of $w_0 = 1$ mm. It is clear that the LG beams with a high radial index maintain the intensity profile in a large propagation distance; namely, such LG beams have a nondiffractive property. This property supports the LG beams with a high radial index as an alternative representation of BG beams, and vice versa [59].

It is also worth noting that the radial variation of the wave front has potential in the application of optical communication; the LG beams with nonzero radial indices could help enlarge the communication capacity. Moreover, the nondiffractive property in a certain short transmission distance is useful for receiving higher signal power, especially when the receiver has a very limited aperture size [63].

3.2 Noncanonical vortices

In addition to the canonical vortices having a helical wave front, noncanonical vortices that carry variable OAMs, such as nonsymmetric vortex beams [64,65], Helico-Conical light beams [66–68], fractional vortex beams [69–

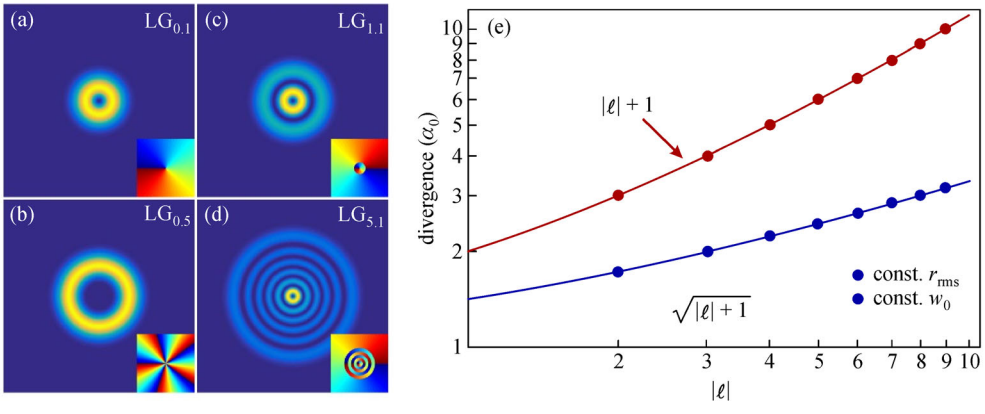

Fig. 1 (a)–(d) Intensity and phase (insets) distributions of canonical vortices; (e) the divergence of vortex beams keeping the Gaussian waist or r_{rms} constant. Two kinds of vortex beams are generated by using forked diffraction grating or cylindrical lens, respectively [58]

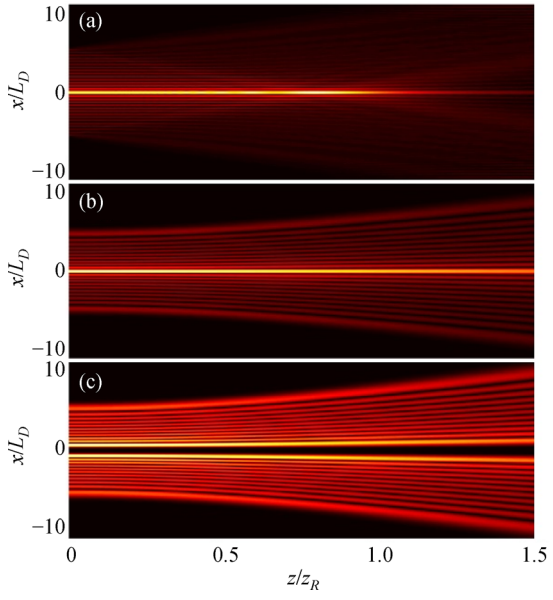

Fig. 2 Evolutions of (a) zeroth-order Bessel beam and LG beams with parameters of (b) l = 0, p = 10 and (c) l = 2, p = 10, respectively

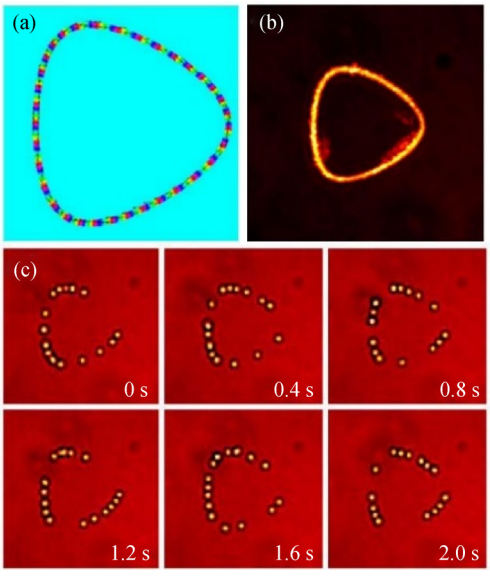

Fig. 3 (a) Phase structure of a triangle vortex with l = 34; (b) beam shape at the focal plane; (c) experimental results of optical tweezer [78]

71], airy vortex beams, and so on, have been proposed with impressive propagation behaviors and practical applications [72–74]. For example, optical vortices with an azimuthally nonuniform phase gradient, including single and multiple singularities, have been successfully created to manipulate the three-dimensional intensity and OAM distributions, especially for engineering the distributions in the vicinity of the focal plane [75–77]. Based on this, optical tweezers that drive colloidal microspheres around quite complicated trajectories have been experimentally implemented [76–79]. Figure 3 shows an optical tweezer based on a noncanonical vortex possessing a triangle phase structure with l = 34 [78]. Moreover, the beams having Helico-Conical phase structures, of which both phase and amplitude express a helical profile as the beam propagation, have demonstrated their capacity to maintain high photon concentration even at higher values of topological charge [68].

The novel propagation dynamics of noncanonical vortices can be expected and explained by the local spatial frequencies [67,79]. For a generic light beam having a field described as $E(x,y) = E_0(x,y)\exp[\mathrm{i}\psi(x,y)]$, where E_0 and ψ are the transverse amplitude and phase distributions, respectively, the local spatial frequencies are given as [67,79]

$$f_x = \frac{1}{2\pi}\frac{\partial}{\partial x}\psi(x,y),$$

$$f_y = \frac{1}{2\pi}\frac{\partial}{\partial y}\psi(x,y). \tag{8}$$

According to Eq. (8), the frequency mapping to the far-field can be plotted, which provides an intuitive mapping for the intensity distribution. Here, we take the vortex beam having an azimuthally nonuniform phase gradient as example, of which the phase is described as $\psi(r,\phi) = 2\pi l(\phi/2\pi)^n$, where n is an integer. The corresponding local spatial frequencies are thus given as [79]

$$f_x = \frac{nl\phi^{n-1}\sin\phi}{(2\pi)^n r},$$

$$f_y = \frac{nl\phi^{n-1}\cos\phi}{(2\pi)^n r}. \tag{9}$$

According to Eq. (9), the mapping (f_x, f_y) to the far-field can be plotted. Figure 4(a) shows the calculated local spatial frequency mapping for the case of n = 3, l = 7, and r = 1. Obviously, the curve represents an Archimedes spiral [79].

In this principle, we attach this noncanonical vortex phase onto the autofocusing Airy beams (AABs) [79], which maintain cylindrical intensity profiles as beam propagation, to modulate their evolution and focusing properties. Figure 4(b) shows the experimentally obtained intensity distribution in the focal plane. It is clear that the experimental result is coincident with the corresponding frequency map; that is, AAB yields to the propagation trajectory depicted in Fig. 4(a).

Figure 5 shows the simulation results including the side view of the AAB propagation at the y-z plane and the intensity distributions at different propagation distances near the focal points. AAB has parameters of l = 8 and n = 2. Compared with the smooth focusing behavior of AABs carrying classical OAMs [80–83], the light energy

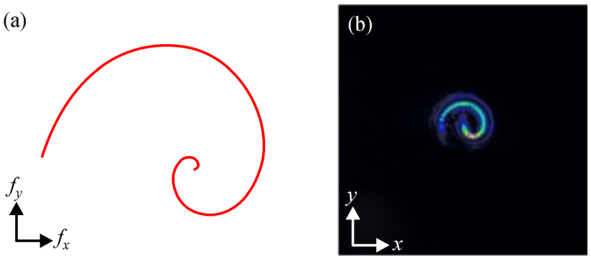

Fig. 4 (a) Local spatial frequencies mapping to the focal field; (b) focal filed intensity of AAB with a power-exponent-phase vortex [79]

gradually converges, and the intensity presents slight oscillation when close to the focal point, as shown in Figs. 5(b)–5(e). This remarkable spiral focusing demonstrates that arbitrary manipulation on the propagation dynamic of light fields can be realized by engineering the locally spatial frequencies.

Further, we introduce variant OAMs into vector AABs to realize the combined manipulation on intensity and polarization distributions in the focal plane of vector fields [84]. Based on the local spatial frequency shown in Eq. (8), we realized intriguing abrupt spin-dependent splitting of vector AABs by encoding cosine-azimuthal variant vortex phases. For a vector AAB with a cosine-azimuthal variant phase, the electric field can be described by the superposition of two spin components as follows:

$$\begin{aligned}\boldsymbol{E}(r,\phi) &= E_0(r)[\cos(m\phi)\boldsymbol{e}_x + \sin(m\phi)\boldsymbol{e}_y]\exp(\mathrm{i}\cos n\phi)\\ &= E_0(r)\{\exp[-\mathrm{i}(m\phi - \cos n\phi)\boldsymbol{e}_L]\\ &\quad + \exp[\mathrm{i}(m\phi + \cos n\phi)\boldsymbol{e}_R]\},\end{aligned} \tag{10}$$

where $E_0(r) = \mathrm{Ai}[(r_0 - r)/w]\exp[\alpha(r_0 - r)/w]$, $\mathrm{Ai}(\cdot)$ denotes the Airy function, r_0 is the radius of the primary ring, w is a scaling factor, α is the exponential decay factor, m is the polarization order, and $\boldsymbol{e}_\mathrm{L} = [1, +\mathrm{i}]^\mathrm{T}/\sqrt{2}$ and $\boldsymbol{e}_\mathrm{R} = [1, -\mathrm{i}]^\mathrm{T}/\sqrt{2}$ are the unit vectors of the left- and right-handed circular polarizations, respectively. According to Eq. (10), two spin components have distinct phase structures—i.e., $\psi_{\mathrm{R,L}} = \pm(m\phi \pm \cos n\phi)$, respectively. According to Eq. (8), the local spatial frequencies in the cylindrical coordinate system are given as

$$\mathbf{L}: \begin{cases} f_\rho = \dfrac{1}{2\pi r}\left|m + n\left(\sin n\phi\cos\dfrac{n\pi}{2} + \cos n\phi\sin\dfrac{n\pi}{2}\right)\right|, \\ \phi = \varphi - \dfrac{\pi}{2}, \end{cases} \tag{11a}$$

$$\mathbf{R}: \begin{cases} f_\rho = \dfrac{1}{2\pi r}\left|m - n\left(\sin n\phi\cos\dfrac{n\pi}{2} - \cos n\phi\sin\dfrac{n\pi}{2}\right)\right|, \\ \phi = \varphi + \dfrac{\pi}{2}. \end{cases} \tag{11b}$$

Considering the parity of phase parameter n, we divided the relationship between local spatial frequencies of two spin states into two cases. For an odd n, the local spatial frequencies have an identical closed-form expression, indicating two spin components presenting the same profile. When n is even, owing to the complementarity of trigonometric functions, the mapping corresponding to local spatial frequencies of two spin components are spaced from each other along the azimuthal direction.

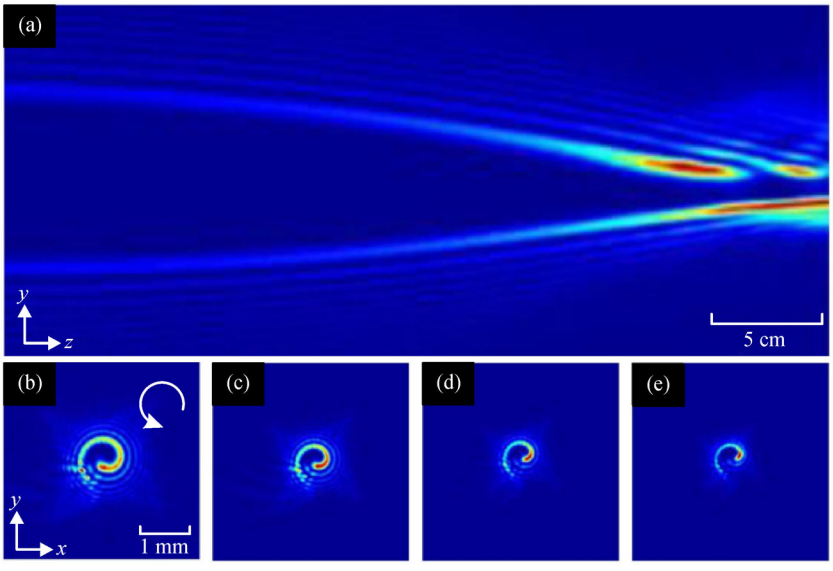

Fig. 5 (a) Side view of propagation dynamic (in y-z plane) of AAB with $l = 8$ and $n = 2$; (b)–(e) intensity distributions at different propagation distances of $z = 19.52$, 20.50, 21.48 and 22.45 cm, respectively [79]

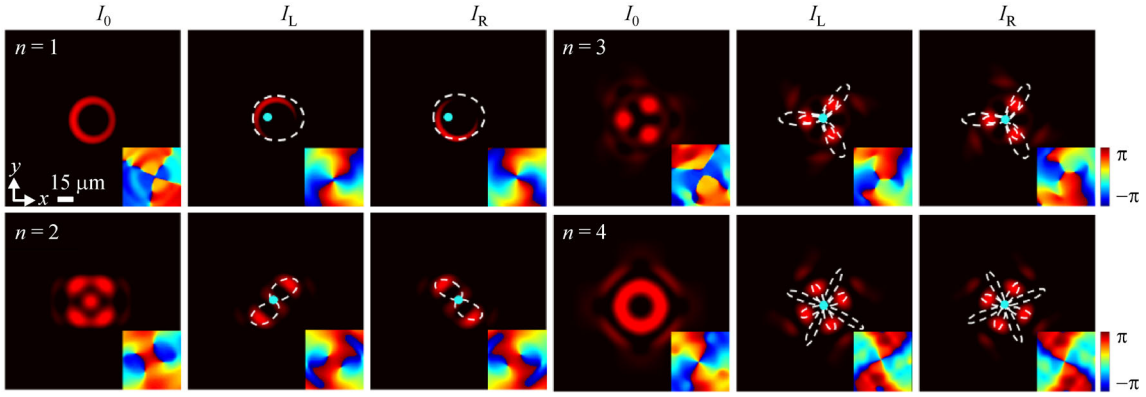

Fig. 6 Simulation intensity distributions of vector AAB with polarization order $m = 2$ and different phase parameters n in the focal plane. I_0, I_L and I_R correspond to the total intensity, left- and right-handed spin components, respectively. The insets represent the phase profiles. The dashed curves denote the local spatial frequencies distributions [84]

Figure 6 displays the intensity distributions of vector AAB with polarization order $m = 2$ and different phase parameter n in the focal plane. In agreement with the theoretical expectation, the vector AABs exhibit distinct focusing behavior with respect to the parity of parameter n. It is noteworthy that when n is odd, although the local spatial frequencies of two spin components have identical spatial distributions, opposite transverse energy flux arising from the phase terms $\exp(\pm im\phi)$ leads to nonuniform intensity distributions. As a result, two spin components would not overlap with each other completely, leading to a transverse spin-dependent splitting.

As discussed above, according to the close mapping relationship between local spatial frequency and the geometrical shape of the focal field intensity distribution, we can consciously control the focusing of two spin components and further manipulate the transverse spin-dependent splitting and phase distributions of the arbitrary vector field by engineering phases corresponding to two spin components [85].

4 Modulation of PB phases on the vector fields

4.1 PB phases

So far, the generation method of vector fields can be divided into two categories: 1) interference superposition of light fields with different polarizations [86–88]; 2) polarization transformation from spatial modulator, such as inhomogeneous wave plate or polarizer, liquid crystal plate, subwavelength grating and metasurface [89–95]. The first one can generate vector fields with an arbitrary complex polarization distribution, whereas the latter is convenient and efficient. These two methods both arise from the phase modulation of two spin states — i.e., the spin–orbital interaction [96,97]. Here, we take the latter method as an example. We suppose that the wave plate has a spatial variant optical axis denoted as $\varphi(x,y)$, with transmission rate $t(x,y) = 1$. Thus, the Jones matrix of the inhomogeneous wave plate can be expressed as

$$M = \begin{bmatrix} \cos 2\varphi & \sin 2\varphi \\ \sin 2\varphi & -\cos 2\varphi \end{bmatrix}. \tag{12}$$

For a left-handed circularly polarized field (or right-handed circularly polarized field) with $E_{in} = E_0 \boldsymbol{e}_L$ ($E_{in} = E_0 \boldsymbol{e}_R$), after passing through this inhomogeneous wave plate, the transmitted field has complex amplitude and polarization denoted as $\boldsymbol{E}_{out} = \boldsymbol{M} \cdot \boldsymbol{E}_{in} = E_0 \exp(i2\varphi)\boldsymbol{e}_R$ [$\boldsymbol{E}_{out} = E_0 \exp(-i2\varphi)\boldsymbol{e}_L$ for the right-handed polarized one]. Therefore, two spin states have distinct responses; that is, two spin states acquire additional geometric phases denoted as $\psi_L = 2\varphi(x,y)$ and $\psi_R = -2\varphi(x,y)$, respectively. These special geometric phases arising from polarization transformation are also called the PB phase [98].

Figure 7 schematically shows the PB phase generation during polarization transformation; the inset illustrates the polarization transformation process on the Poincaré sphere. A focused Gaussian beam with linear polarization A passes through an inhomogeneous optical system (or wave plate), which imposes PB phases ψ_L and ψ_R onto two spin components, changing its polarization state to B [99]. Supposing the incident beam has the field distribution $E = E_0[a\exp(-i\phi_0)\mathbf{e}_L + b\exp(i\phi_0)\mathbf{e}_R]/\sqrt{2}$, the output thus can be described as

$$\boldsymbol{E} = E_0\{a\exp[i(\psi_L - \phi_0)e_R] + b\exp[i(\psi_R + \phi_0)\boldsymbol{e}_L]\}/\sqrt{2}. \tag{13}$$

Equation (13) indicates that by utilizing the spatially inhomogeneous PB phases, one can conveniently reshape the wave front without changing the intensity profile immediately after the polarization transformation optical system. Based on this result, various optical elements with

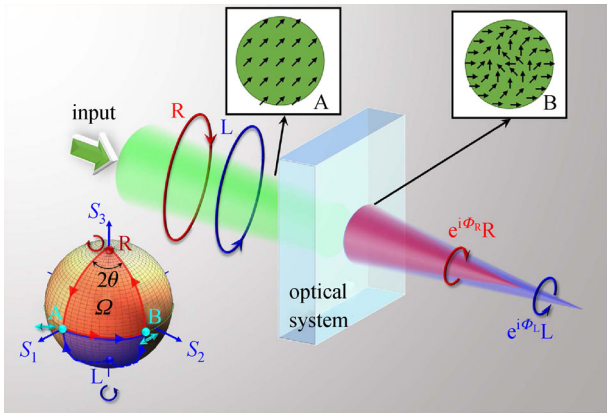

Fig. 7 Schematic illustration of PB phases generation in the process of polarization transformation. Insert: schematic illustration of polarization transformation on the Poincaré sphere [99]

architectures including patterned subwavelength grating, liquid crystal, and metasurface have been broadly used to generate vector beams.

In addition to the standard Poincaré sphere shown in Fig. 7, other kinds of Poincaré spheres have been proposed to represent the inhomogeneous polarization states [100–103], such as the higher-order Poincaré spheres composed of two opposite spin states with opposite spiral phases [100] and the hybrid-order Poincaré sphere composed of two opposite spin states with different spiral phases [102]. For these cases, the resulting PB phases of two spin components are closely related with the topological charges and spin assigned to the sphere [100,102].

4.2 Polarization singularity conversion

The PB phase, in turn, supports an approach to manipulate the propagation dynamics of two spin states because of the corresponding relationship between the phase gradient structures in position space and wave vector in momentum space. Utilizing tailored PB phases, some intriguing manipulations of spin states in three dimensions, involving spin-orbital interaction, spin Hall effect of light (SHEL), and light-guiding confinement, have been implemented [104–109].

The most common PB phases are the canonical vortex phases—i.e., $2\varphi = \pm l\phi$—which transform an incident Gaussian beam with linear polarization into a cylindrical vector beam [86,88,105]. In such cases, two spin components carrying opposite OAMs exhibit identical diffraction, as mentioned in Section 3.1. As a result, the vector beam maintains its polarization state with a slowly varying intensity profile upon propagation. Nevertheless, when $l_R \neq l_L$, two spin components exhibit obvious divergence during beam propagation [110,111]. Owing to the cylindrical symmetry, the divergence leads to spin-dependent separation along the radial direction. Considering the total field output from the optical system (or wave plate), one can see that it is a cylindrical vector vortex beam characterized by parameters $m = (l_L - l_R)/2$ and $l = (l_L + l_R)/2$. Here, m and l are the polarization order and topological charge of the additional vortex phase, respectively. On the other hand, as a whole, under the modulation of an additional OAM, the vector fields exhibit spin-dependent splitting upon propagation. Therefore, this phenomenon is also called the radial SHEL. Shu et al. realized such radial spin-dependent splitting by using a dielectric metasurface with a radially varying optical axis [112].

For the vector vortex field with larger OAM, more obvious divergence occurs, resulting in more serious polarization distortion [111]. In other words, according to the dependence of the amplitude profile on the topological charge, the vector vortex fields with the same polarization order but different OAMs usually present distinct intensity profiles. To overcome the divergence, we proposed perfect vector vortex beams, which not only have an intensity profile independent of the polarization order and additional OAM but also have a stable intensity profile and polarization at a certain propagation distance [113]. Figure 8 displays the perfect vector vortex beams generated from the superposition of two annular spin components with different vortex PB phases, which are created by the Fourier transformation of Bessel–Gauss beams with an identical transverse wave vector. Here, $|H\rangle$ denotes the state composed of two spin components with OAMs defined by subscripts. The local linear polarization orientation and phase distribution are shown in the third and fourth rows, respectively. Importantly, such vector vortex beams have been demonstrated to have the capacity of maintaining the polarization and intensity profile in a

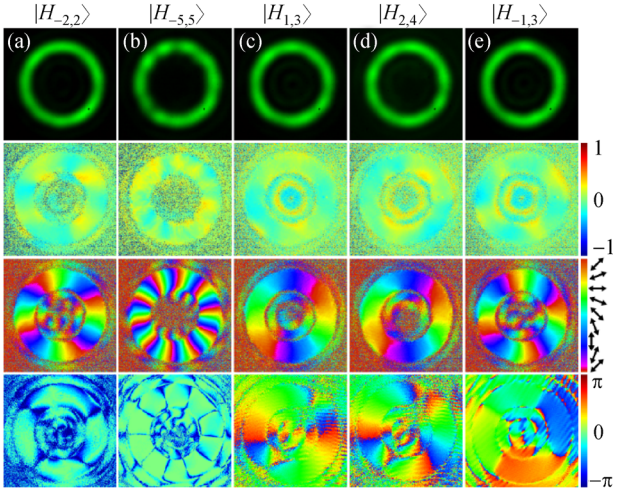

Fig. 8 Distributions of intensity (top row), s_3 (second row), polarization orientation (third row) and phase (bottom row) of different states. $|H\rangle$ denotes the sate composed by two spin components with OAMs defined by subscripts [113]

certain propagation distance [113].

Furthermore, we note that the divergence of two spin components composing the vector field reaches its maximum at the far-field — i.e., $z \to \infty$. Therefore, we explored the divergence by observing the polarization state in the focal plane [114]. Figure 9 shows the numerically calculated results of the intensity and polarization distributions of the focused azimuthally polarized beam carrying vortex phases of l = 1, 2 and 3. The dotted, dashed, and solid lines in the top row depict the zero contours of s_1, s_2, and s_3, respectively; the background and short lines in the bottom row denote the ellipticity and orientation of the polarization ellipse, respectively. The results show that when an additional OAM is attached to the vector beam, the polarization in the focal plane changes dramatically. Moreover, we note that the azimuthally polarized beams focus into radially polarized ones.

According to Eq. (3), one can find that at the focal plane — i.e., $z \to \infty$ — vortex beams have cylindrical intensity profiles, whose size is dependent on their topological charges. In addition, it is notable that the Gouy phases of vortex beams are $\Phi = (|l| + 1)\pi/2$, which means that two spin components composing the vector vortex beam obtain different Gouy phases with respect to their topological charges [115]. If $(|l_L| - |l_R|)/2$ is even, two spin components are in phase within the focal plane, and the focused field has identical polarization orientation with the incident field; if $(|l_L| - |l_R|)/2$ is odd, two spin components have constant phase difference of π, and the overlap area of two spin components consequently presents opposite polarization orientation. For the case shown in Fig. 9(a), the right-handed spin component has the zeroth OAM, so its corresponding focal field has an intensity profile similar to the Gaussian beam; that is, the corresponding focal field presents a solid bright spot in the center point. Accordingly, the incident vector point is transformed into a circularly polarized point. However, for the cases of Figs. 9(b) and 9(c), $(|l_L| - |l_R|)/2 = 1$, the overlap areas are radially polarized. Meanwhile, because of the relationship between the profile size and topological charge, the spin component that has a smaller topological charge dominates the central region. As a result, the vector point is transformed into a circularly polarized point with corresponding chirality.

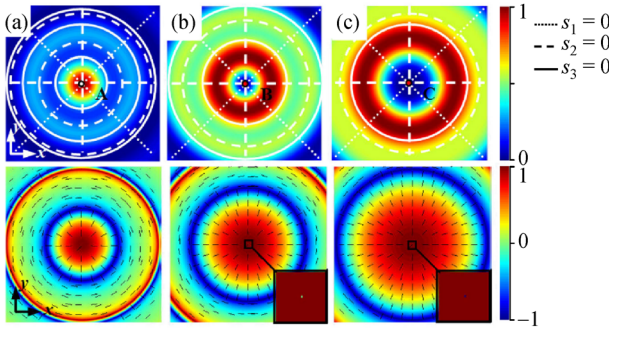

Fig. 9 Intensity and polarization distributions of the focal fields of the azimuthally polarized beams with vortex phases of l = 1, 2 and 3, respectively. The dotted, dashed and solid lines in the top row depict the zero contours of s_1, s_2 and s_3, respectively; the background and short lines in the bottom row denote the ellipticity and the orientation of polarization ellipse, respectively [114]

In addition to the abovementioned beams that slowly change their polarization in the focusing process, we also created vector AABs associated with OAM and experimentally studied the abrupt polarization transitions induced by spin–orbital interaction by engineering the PB phases corresponding to two spin components [116]. Figure 10 displays the autofocusing of radially polarized AABs without and with a single charged vortex phase. From Fig. 10, it is clear that when the polarization order and topological charge of the vortex phase are equal in number, significant polarization singularity conversion occurs, and the local polarizations undergo an abrupt transition from linear to spin states.

4.3 Spin-dependent splitting

The other typical selection of the PB phase is that with a linear function, such as $2\varphi(x,y) = \pm k_x x$ [99,117,118]. For this case, two spin states would obtain two mutually conjugate titled phases and separate transversely with each other upon propagation. This spin-dependent transverse separation was reported by Hasman in 2002 by employing spatially variant subwavelength grating [117,118]. Later, many primary works about the PB phase inducing photonic SHE were carried out. Zhang et al. observed highly enhanced spin-dependent transverse separation by using metasurface composed of metal nano-antenna arrays [108]. Ling et al. reported a giant photonic SHE by using dielectric metasurface fabricated by a femtosecond laser self-assembly nanostructure [119]. In addition to the pure phase information, the phases within which the amplitude information is encoded, such as Hermite–Gauss and Airy modes [120], even the combination of several phases [99], can be selected as PB phases. Figure 11 displays the spin-dependent splitting in the case of $2\varphi(x,y) = \pm(k_x x + \phi)$. The initial beam is depicted in Fig. 11(a). The side view of propagation (Fig. 11(d)) and s_3 distribution (Fig. 11(c)), as well as measured polarization, demonstrate that not only the SAM but also the OAM can be separated merely by engineering PB phases.

Of course, the PB phase can be selected as any phase expected. This means that by steering the PB phases, we can also realize longitudinal spin-dependent splitting. In geometric optics, we realize the convergence and divergence of the beam by using a square phase imparted by a lens. Therefore, we suppose that the linearly polarized incident beam has a convergent phase of $\exp(-i\alpha_0 r^2)$, and the PB phases are $2\varphi(x,y) = \pm(\alpha r^2)$. For such a case, it is

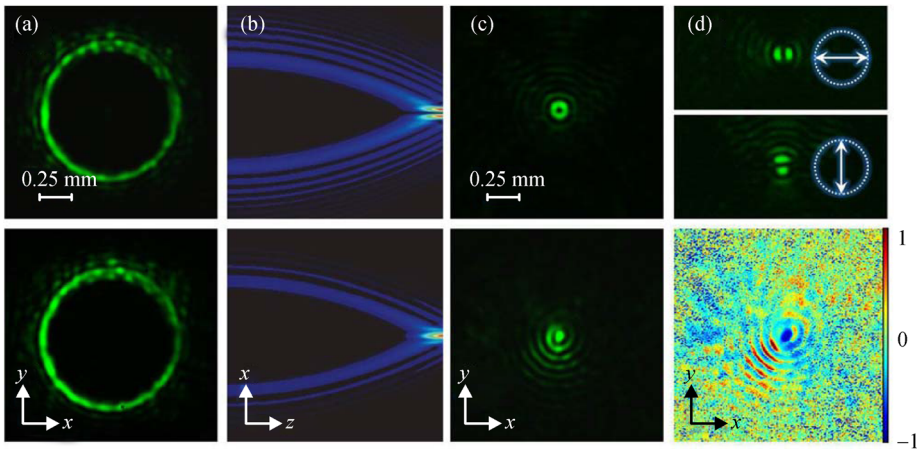

Fig. 10 Autofocusing of radially polarized AABs without (top) and with (bottom) a single charged vortex phase. (a) and (c) depict the beam intensity patterns at input and output, respectively; (b) and (d) side view of the beam propagation from numerical simulation and measured beam polarizations at output [116]

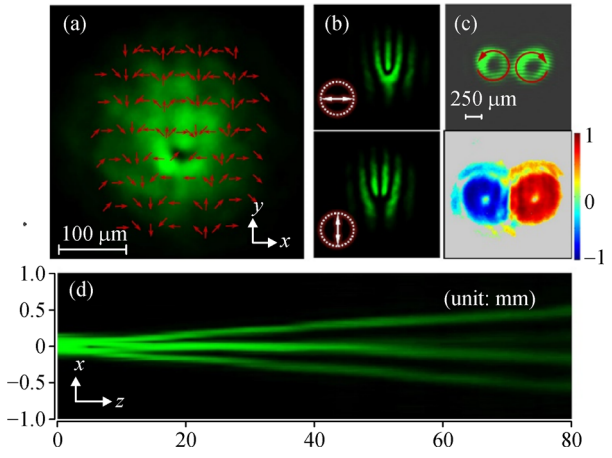

Fig. 11 Spin-dependent separation with the bifurcation of orbital angular momentum. (a) Initial beam with polarization direction marked with red arrowheads; (b) horizontally and vertically polarized components; (c) interference pattern of output beam with a plane wave (top), and the corresponding s_3 distribution (bottom); (d) side view of the beam propagation

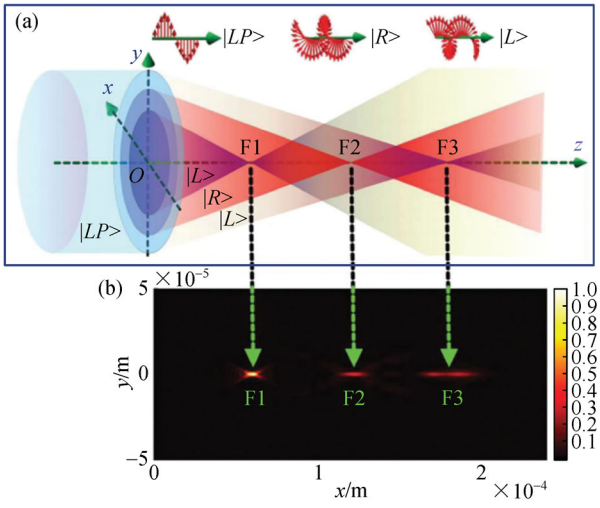

Fig. 12 (a) Schematic illustration of the longitudinal three-foci metasurface lens; each focal point is focused from segmented region with distinct PB phase response; (b) the observed light spots correspond to the three focal points. Adapted from Ref. [127]

clear that two spin components would respectively focus into the focal planes $f(\alpha_0 \pm \alpha)$, resulting in dual-foci in the longitudinal direction — i.e., longitudinal spin-dependent splitting [106,121,122]. By relying on modern fabrication technology, metasurface and other devices with subwavelength thickness enable a PB phase lens, similar to the Fresnel lens [123–126]. Furthermore, a PB phase-based multifocus lens has also been realized by using segmented metasurface [127]. Figure 12 schematically shows the operating principle of a longitudinal three-focus lens. To realize three foci, the metasurface is divided into three annular regions with different PB phases and thereby focus the corresponding incident field to three longitudinal points.

Additionally, by combining this longitudinal spin separation with the transverse one, we experimentally achieved a controllable spin-dependent focal shift in three-dimensional space [99]. When the PB phase is a polynomial as $2\varphi(x,y) = k_x x + k_y y + \alpha r^2$, two spin states hence focus to points (x_R, y_R, z_R) and (x_L, y_L, z_L), respectively. Here, $x_{R,L} = k_x z_{R,L}/k$, $y_{R,L} = k_y z_{R,L}/k$, and $z_{R,L} = f(\alpha_0 \pm \alpha)$. This modulation of special PB phases on the propagation dynamics of spin states reveals a series of intriguing phenomenon. More importantly, it promotes the development of spin-optics and further contributes to application; e.g., this remarkable prospect of spin-dependent separation in holographic imaging has excited new research directions [128,129].

4.4 *z*-dependent polarization

Accompanied by the spin-dependent separation, the light field changes its polarization upon propagation. This special light field with longitudinally variant polarization but an identical transverse intensity pattern during propagation has attracted research interest owing to its application potential in material processing, polarization meteorology, microscopy imaging, optical communication, and so on [106,121]. In 2013, Cardano et al. generated Poincaré beams that rotate the transverse polarization distribution by using spiral wave plates [130]. They transformed part of the incident light field with $LG_{0,0}$ mode and spin state into $LG_{0,l}$ mode with opposite spin state. The transformed $LG_{0,l}$ has a vortex phase axially overlapping with the idle $LG_{0,0}$ mode, resulting in Poincaré beams with Lemon, star, and spiral polarizations that depend on the topological charge of $LG_{0,l}$ mode. As mentioned above, LG modes have a Gouy phase that is closely related to the radial index p and topological charge l. Therefore, two spin states have a longitudinally varying Gouy phase difference — i.e., $\Delta\Phi = |l|\tan^{-1}(z/z_0)$. This z-dependent phase difference leads to the rotation of polarization upon beam propagation.

Remarkably, Moreno et al. reported a kind of vector Bessel beam that changes transverse polarization upon propagation — i.e., vector Bessel beams having z-dependent polarization [131,132]. Combining the vortex phase with axicon phases, one can create two-dimensionally varying PB phases with different periods for two orthogonal polarizations — e.g., $\psi_{R,L}(r,y) = \pm l\phi + (k_r \pm k_0)r$. In this principle, we construct vector beams with transverse varying polarization and further generate zeroth- and higher-order Bessel beams with z-dependent polarization by employing the linear focusing of the axicon [133]. Figure 13 shows a schematic representation of z-dependent polarization distribution and transformation as well as experimentally measured intensity distributions of vertically polarized components at different planes. It is seen that the first-order vector Bessel beam longitudinally varies its local polarization upon propagation. Overall, the Bessel beam presents three-dimensionally variant polarization.

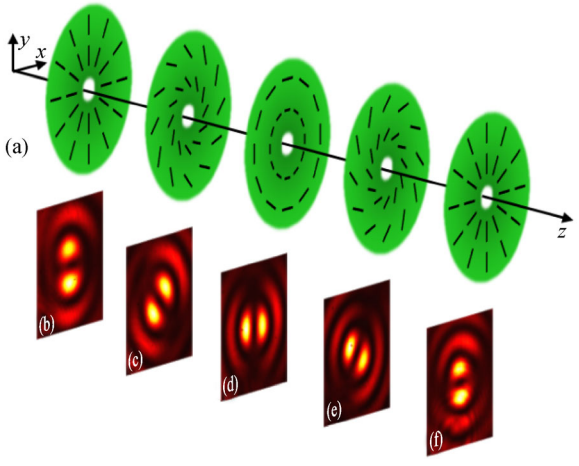

Fig. 13 Schematic representation of z-dependent polarization distribution and transformation; (b)–(f) experimentally measured intensity distributions of first-order Bessel beam propagating through a vertical polarizer at planes with equal space [133]

Furthermore, we explored the self-healing of these vector Bessel beams, including the transverse intensity profile and the three-dimensional polarization structure, by observing their transverse intensity and Stokes parameter distributions after propagating through two disparate obstacles. Figure 14 shows the measured reconstruction of second-order vector BG beams after a linear obstacle. Importantly, as the results show in Fig. 14, the three-dimensional polarization property can be reconstructed after such an obstacle. The degree of longitudinal variation in polarization and the self-healing can address many application challenges. For example, by combining it with the polarization response property of anisotropic material, these beams can be used for material processing at a special depth and to improve the axial resolution in 3D imaging. To some extent, the higher-order Bessel beams supporting quantitative OAM and SAM simultaneously, with z-dependent polarization, may induce intriguing phenomena such as SAM-OAM conversion and spin transport.

5 Modulation of OAMs on the azimuthally broken fields

5.1 Vortex beams

The canonical vortex beam manifests itself as the helical phase, which generally has rotation symmetry. The transverse OAMs accordingly are null for such beams. However, as discussed in Section 3.2, the noncanonical vortex phases break this rotation symmetry and thereby produce transverse energy flow, leading to the variation of beam profile during propagation. It is natural to expect that by breaking the rotation symmetry, one can consequently introduce nonzeroth transverse OAM, then create abundant intensity structures. On the other hand, research on broken beams has demonstrated an important effect in information reconstruction [134]. Therefore, increasing attention has been devoted to the nonsymmetric optical vortices [135–140].

Remarkably, in the azimuthally broken vortex beams — namely, fan-shaped vortex beams — the transverse energy flow induced by the phase gradient gradually transfers the energy to the opaque region upon beam propagation [135]. The diffraction of fan-shaped vortex beams can be interpreted based on the angular diffraction theory [141–143]. Supposing that a fan-shaped mask has a sector photic region, the transmission function can be expressed as [144,145]

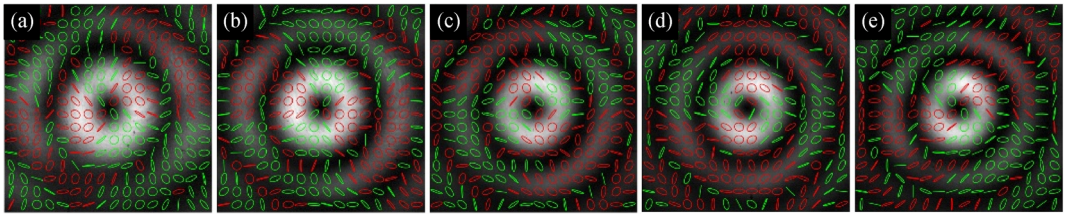

Fig. 14 Measured transverse intensity and local polarization distributions of the reconstructed second-order BG beam with hybrid polarizations at propagation distances of z = 21, 23.8, 26.6, 29.5, 32.2 cm, respectively. The red and green ellipses denote the RH and LH elliptical polarizations, respectively. The linear obstacle with a diameter of about D = 70 μm is placed at plane z = 16.6 cm [133]

$$P(\phi)=\begin{cases} t, & -\beta/2\leqslant\varphi\leqslant\beta/2, \\ 0, & \text{else}, \end{cases} \tag{14}$$

where β is the angle width of the fan-shaped aperture, and t is the transmission of the photic region. Here, we set t = 1, and the incident vortex beam has complex amplitude denoted as $E=\exp(-r^2/w^2)\exp(\mathrm{i}l\phi)$, where w is the waist of the Gaussian background. According to the angular diffraction theory, the photic region is analogous to an angular grating with 2π periodic nature. The complex transmission of the angle distribution can be expressed in terms of the angular momentum distribution with a Fourier coefficient as follows [144,145]:

$$E(r,\phi)=\frac{\beta}{2\pi}\exp\left(-\frac{r^2}{w^2}\right)\sum_{n=-\infty}^{+\infty}\mathrm{sinc}\left(\frac{n\beta}{2}\right)\exp[\mathrm{i}(l+n)\phi], \tag{15}$$

where n is an integer. From Eq. (15), one can find that after passing through the aperture, the incident beam splits into a series of OAM spectra, which are characterized by the topological charges of $l+n$. In consequence, the diffraction of the vortex beam can be described by the superposition of diffractive OAM spectra.

For each OAM spectrum that follows the paraxial approximation, its evolution can be described by the Fresnel diffraction as

$$\begin{aligned} E_n(\rho,\theta)=&\frac{-\mathrm{i}\beta}{2\pi\lambda z}\mathrm{sinc}\left(\frac{n\beta}{2}\right)\exp\left(\frac{\mathrm{i}k\rho^2}{2z}\right) \\ &\iint\exp\left(-\frac{r^2}{w^2}\right)\exp\left(\frac{\mathrm{i}kr^2}{2z}\right) \\ &\times\exp[\mathrm{i}(l+n)\phi]\exp\left[-\frac{\mathrm{i}kr\rho\cos(\theta-\phi)}{z}\right]r\mathrm{d}r\mathrm{d}\phi, \end{aligned} \tag{16}$$

where (ρ,θ,z) are the cylindrical coordinates. With the help of Bessel integration, we can obtain the diffractive fields as [145]

$$E(\rho,\theta)=u(\rho,z)\mathrm{e}^{\mathrm{i}\Delta\Phi}\sum_{n=-\infty}^{+\infty}\mathrm{sinc}\left(\frac{n\beta}{2}\right)A_{l+n}(\rho,z)\mathrm{e}^{\mathrm{i}(l+n)(\theta-\pi/2)}, \tag{17}$$

with

$$A_{l+n}(\rho,z)=[I_{(l+n-1)/2}(\gamma)-I_{(l+n+1)/2}(\gamma)]\exp\left(-\frac{1}{2}\frac{\rho^2}{w(z)^2}\right)\frac{\rho}{w_0}, \tag{18}$$

where $\Delta\Phi=3\pi/4-3\tan^{-1}(z/z_0)/2+zz_0(\rho/w_0)^2/(z^2+z_0^2)$ denotes the dynamic phase, $I_v(\gamma)$ is the modified Bessel function of the first kind of order v, $\gamma=\rho^2(1+\mathrm{i}z_0/z)/2w_z^2$, $w_z=w_0[1+(z/z_0)^2]^{1/2}$ is the beam waist at propagation distance z, and $z_0=kw_0^2/2$ is the Rayleigh length. All nonessential factors are absorbed into the envelope profile: $u(\rho,z)=(\rho\beta/4\pi w_0)(z_0/z)^{5/4}(z_0/R_z)^{3/4}\exp[-\mathrm{i}(\pi-\theta_0)/2]$, where $R_z=z[1+(z_0/z)^2]$ is the radius of curvature for the wave front.

According to Eqs. (17) and (18), we calculate the diffractive fields by numerically solving the above two equations. Intuitively, after propagating a distance z, the angular position of the peak intensity experiences angular rotation, which depends on l. Figure 15 presents the relationship between rotation angle and topological charge, as well as the intensity distribution of l = –4 and –20 vortex beams at z = 0 and 25 cm planes, respectively, with the parameters selected as λ = 532 nm, w_0 = 1 mm [145]. In Fig. 15(a), the solid curve corresponds to the result calculated from Eqs. (17) and (18), and the blue and red squares correspond to the measured results of the two spin states. It is discernible that the fan-shaped vortex beams undergo rotation during diffraction. Importantly, the rotation angle increases with increasing topological charge. Figure 15(d) shows the intensity distributions of $l=\pm20$ vortex beams after propagating 25 cm. The red and blue lines correspond to the l = 20 and –20 order vortex beams. It is quite clear that the vortex beams having equal modulus of topological charges rotating equally along the opposite azimuthal direction. This l-dependent rotation can also be intuitively described by the transverse OAM flow, which is proportional to the azimuthal gradient of the vortex phase.

Owing to the transverse energy flow, it is naturally seen that the rotation increases with increasing propagation

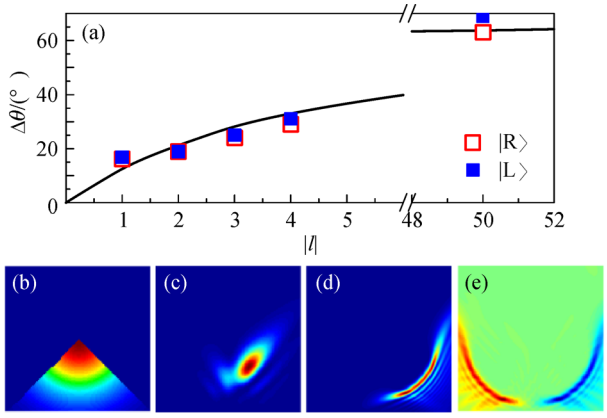

Fig. 15 (a) Rotation angles $|\Delta\theta|$ versus the topological charges; (b)–(e) Intensity distributions of fan-shaped vortex beams at $z = 0$ and 25 cm planes. (c) $l = -4$; (d) $l = -20$; (e) $l = \pm 20$. $|R\rangle$ and $|L\rangle$ correspond to two spin states. The red and blue areas correspond to the positive and negative vortex beams, respectively

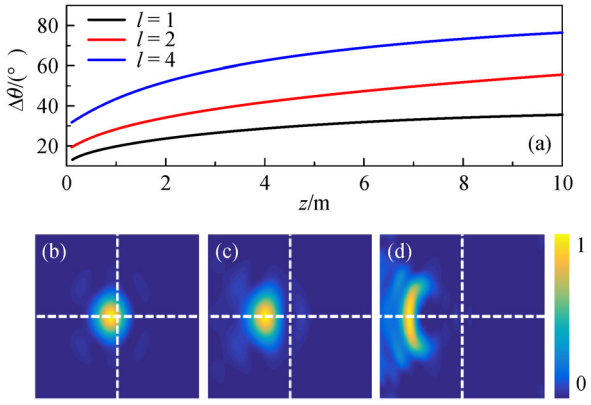

Fig. 16 (a) Rotation angles $|\Delta\theta|$ versus propagation distance z. (b)–(d) Focal intensity distributions of $l = 1$, 4 and 20 fan-shaped vortex beams with $\beta = \pi/2$, respectively. The incident fan-shaped vortex beams have the same profile as shown in Fig. 15(b)

distance [145]. Figure 16(a) shows the relationships between rotation angle $|\Delta\theta|$ and propagation distance for three topological charge vortex beams, according to Eqs. (17) and (18). As expected, the rotation angle increases with increasing propagation distance. Particularly, at the far-field — i.e., $z \to \infty$ — from Eq. (17) and (18), and it can be concluded that the complex amplitudes $A_{l+n}(\rho,z)$ become real values. Meanwhile, the nth-order OAM spectrum has a constant phase retardation $(l + n)(\theta - \pi/2)$. This means that the OAM spectra are in phase and constructively interfere at azimuthal position $\theta + \pi/2$; namely, the fan-shaped rotates to azimuthal position $\theta = \pi/2$. Figures 16(b)–16(d) display the focal intensity distributions of $l = 1$, 4, and 20 fan-shaped vortex beams with $\beta = \pi/2$, respectively. The incident fan-shaped vortex beams have the same profile as shown in Fig. 15(b).

The propagation of a fan-shaped scalar vortex beam in the paraxial limit has been reported, showing that the intensity pattern is rotated with beam propagation, and the direction of the rotation depends on the sign of the topological charge. This phenomenon can be attributed to the spiral phase shift of the beam. For fan-shaped Bessel–Gauss beams that have remarkable features of nondiffraction and self-healing, the spatial intensity distributions at the focal plane were well recovered [140,146,147].

5.2 Vector beams

By breaking the rotation symmetry, vector fields also produce redistributed intensity, polarization, and OAM during propagation. Figure 17 displays the measured s_3 distributions of fan-shaped pure cylindrical vector (CV) beams with $\beta = \pi/2$ in the planes of $z = 25$ cm and $z \to \infty$ (the focal plane of a lens). The red and blue areas correspond to the right- and left-handed spin components, and the dashed areas schematically show the incident

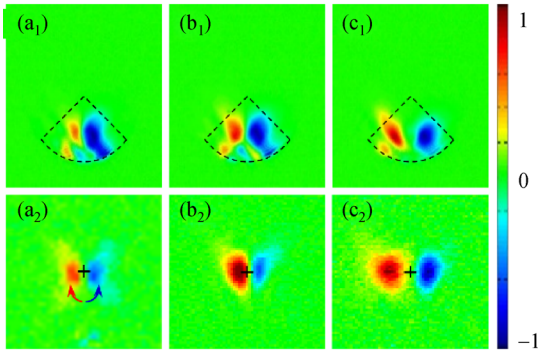

Fig. 17 Measured s_3 distributions of fan-shaped pure CV beams with $\beta = \pi/2$ in the planes of $z = 25$ cm (upper row) and $z \to \infty$ (the focal plane of a lens, below row). The red and blue areas correspond to the right- and left-handed spin components, the dashed areas schematically show the incident beams. The polarization orders are $m = 1$, 2 and 4, respectively

beams. The polarization orders are $m = 1$, 2, and 4, respectively. It is clear that the two spin components represent opposite angular rotation– i.e., angular splitting — which is also regarded as the angular SHEL [148]. For a pure CV beam, $l_L = -l_R = m$ and $l = 0$, the photonic SHE value is $2|\Delta\theta|$. Intuitively, the spin-dependent splitting reaches its maximum at the far-field. Wang et al. reported the focal field characteristics of fan-shaped azimuthally polarized beams and revealed the focusing mechanism of such beams [138].

Based on this, we introduced the rotation symmetry of a fan-shaped aperture and then investigated the focal fields of azimuthally polarized beams with multiple fold rotation symmetry [144,149]. The focusing mechanism is schematically shown in Fig. 18. Each fan-shaped lobe of the vector beam creates a pair of spin components, which rotate $\pm\pi/2$ at the focal plane. As a result of the interferential

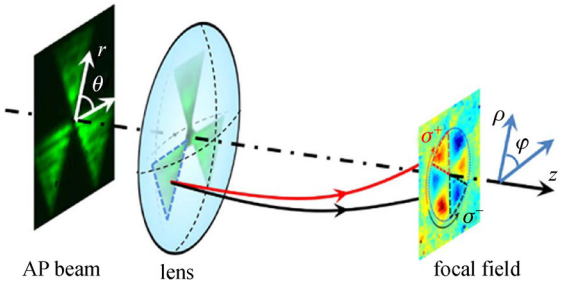

Fig. 18 Schematic illustration of the focusing dynamics of a fan-shaped azimuthally polarized beam [149]

superposition of spin components focusing from several lobes, the focal field redistributes the polarization, intensity, and OAM. Remarkably, we found that the focal field focused from azimuthally polarized beams with odd- and even-fold symmetries are significantly different.

Figure 19 shows the intensity and s_3 distributions in the focal fields of azimuthally polarized beams with odd- and even-fold symmetries. For the beam with even-fold rotation symmetry, it consists of even lobes. According to the results in Figs. 17 and 18, two lobes with opposite angle positions in the pupil plane create two spin components carrying opposite OAMs and SAMs at the same angle position in the focal plane. The superposition of two spin components consequently results in locally linear polarization. However, for the odd-fold beams, the spin components focused from each lobe cannot overlap at that same angle position in the focal plane, resulting in a special focal field with complex polarization and energy flow, as show in Figs. 19(a), 19(c), and 19(e).

5.3 Vector vortex fields

For a generic vector vortex beam having mth-order polarization and $l\hbar$ OAM, these two spin components accordingly have topological charges of $l_L = l + m$ and $l_R = l - m$, respectively. After the spatial modulation of the fan-shaped aperture with angle width of β, two spin components undergo angular diffraction with respective to the topological charges l_L and l_R. As shown in Fig. 15, the angular diffraction of the vortex beams is closely related to the carried OAMs. Therefore, by introducing an additional OAM into broken vector beams — namely, setting $l_L \neq l_R$ — one can produce asymmetric rotation and then steer the angular spin-dependent splitting [145,148].

Based on this principle, we reported a new photonic SHE for a freely propagating fan-shaped vector vortex beam in a paraxial situation [145]. Figure 20 shows the asymmetric spin-dependent splitting of fan-shaped vector vortex beams with constant polarization order. The polarization order is $m = 2$, and the propagation distances are about 25 cm. The topological charges of the vector vortex beams are $l = 2$, -1, and 3, respectively. The angle width in all three cases is $\beta = \pi/2$. For the case of $l = m = 2$, the right-handed spin component does not undergo rotation because of its zero OAM, whereas the left-handed spin component rotates approximately 35°. Particularly, for the case shown in Fig. 20(c), $l_R = 1$ and $l_L = 5$, two spin components can rotate along the same angular direction. The results provide us with a direct way to manipulate the photonic SHE of a vector beam, including magnitude and orientation. Moreover, we can also change the photonic SHE by altering the shape of the vector vortex beam — namely, the size of the fan-shaped aperture [148].

6 Conclusions

Since Allen reported that the LG modes carry OAMs, a great variety of studies have been devoted to exploiting OAM, including the paraxial and nonparaxial propagation in homogeneous and inhomogeneous materials, as well as linear and nonlinear systems. These works have greatly developed the practical applications, evolving optical tweezers, optical and quantum communication, super-resolution microscopy and lithography, and high-precision measurements. Furthermore, the theories on optical vortices have been successfully expanded to electric

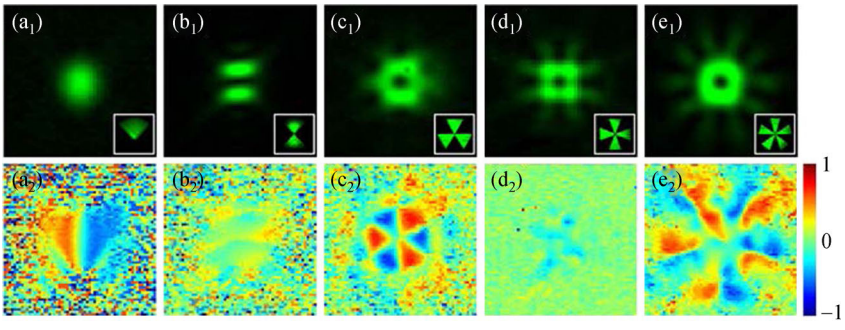

Fig. 19 Distributions of intensity and s_3 in the focal field of azimuthally polarized beams with different rotation symmetries. Insets: the intensity distributions of beams in the pupil plane [149]

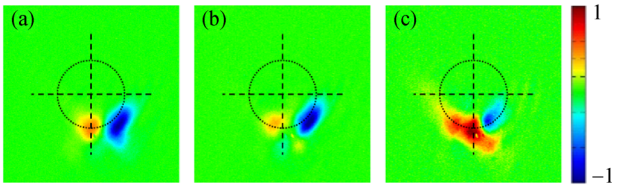

Fig. 20 Distributions of s_3 for fan-shaped beams with angular width of $\pi/2$, after propagating 25 cm. (a) $m = 2$, $l = 2$; (b) $m = 2$, $l = -1$; (c) $m = 2$, $l = 3$ [145]

beams, atom beams, and even matter wave systems. The study of OAM is still in its infancy.

Here, we have selectively focused on novel evolutions of beams carrying OAM and given an overview of the modulations of OAM on the propagation dynamics of scalar and vector beams in free space. We first introduced the evolutions of canonical and noncanonical vortex beams. Subsequently, we reviewed the Pancharatnam–Berry phases arising from spin-orbital interaction and presented novel behavior such as spin-dependent splitting, polarization singularity conversion, and z-dependent polarization. We further discussed the propagation and focusing properties of azimuthally broken vector vortex beams. New ideas and developments are emerging at a rapid pace, and it is clear that the OAM will provide new opportunities for topological photonics, spin-photonics, and spintronics.

Acknowledgements This work was funded by the National Natural Science Foundation of China (NSFC) (Grant Nos. 11634010, 11404262, 61675168, U1630125 and 61377035); Fundamental Research Funds for the Central Universities (No. 3102015ZY057); and Innovation Foundation for Doctor Dissertation of North-western Polytechnical University (No. CX201629).

References

1. Poynting J. The wave motion of a revolving shaft, and a suggestion as to the angular momentum in a beam of circularly polarised light. Proceedings of the Royal Society of London. Series A, Containing Papers of a Mathematical and Physical Character, 1909, 82(557): 560–567
2. O'Neil A T, MacVicar I, Allen L, Padgett M J. Intrinsic and extrinsic nature of the orbital angular momentum of a light beam. Physical Review Letters, 2002, 88(5): 053601
3. Barnett S M, Allen L, Cameron R P, Gilson C R, Padgett M J, Speirits F C, Yao A M. On the natures of the spin and orbital parts of optical angular momentum. Journal of Optics, 2016, 18(6): 064004
4. Allen L, Beijersbergen M W, Spreeuw R J, Woerdman J P. Orbital angular momentum of light and the transformation of Laguerre-Gaussian laser modes. Physical Review A, Atomic, Molecular, and Optical Physics, 1992, 45(11): 8185
5. He H, Friese M E, Heckenberg N R, Rubinsztein-Dunlop H. Direct observation of transfer of angular momentum to absorptive particles from a laser beam with a phase singularity. Physical Review Letters, 1995, 75(5): 826–829
6. Allen L, Padgett M, Babiker M I V. The orbital angular momentum of light. Progress in Optics, 1999, 39: 291–372
7. Padgett M, Allen L. The Poynting vector in Laguerre-Gaussian laser modes. Optics Communications, 1995, 121(1–3): 36–40
8. Curtis J E, Grier D G. Structure of optical vortices. Physical Review Letters, 2003, 90(13): 133901
9. Berkhout G C, Lavery M P, Courtial J, Beijersbergen M W, Padgett M J. Efficient sorting of orbital angular momentum states of light. Physical Review Letters, 2010, 105(15): 153601
10. Franke-Arnold S, Allen L, Padgett M. Advances in optical angular momentum. Laser & Photonics Reviews, 2008, 2(4): 299–313
11. Onoda M, Murakami S, Nagaosa N. Hall effect of light. Physical Review Letters, 2004, 93(8): 083901
12. Bliokh K Y, Bliokh Y P. Conservation of angular momentum, transverse shift, and spin Hall effect in reflection and refraction of an electromagnetic wave packet. Physical Review Letters, 2006, 96(7): 073903
13. Hosten O, Kwiat P. Observation of the spin hall effect of light via weak measurements. Science, 2008, 319(5864): 787–790
14. Bliokh K Y, Smirnova D, Nori F. Quantum spin Hall effect of light. Science, 2015, 348(6242): 1448–1451
15. Liu Y C, Ke Y G, Luo H L, Wen S C. Photonic spin Hall effect in metasurfaces: a brief review. Nanophotonics, 2017, 6(1): 51–70
16. Bliokh K Y, Rodríguez-Fortuño F J, Nori F, Zayats A V. Spin-orbit interactions of light. Nature Photonics, 2015, 9(12): 796–808
17. Bliokh K Y, Shadrivov I V, Kivshar Y S. Goos-Hänchen and Imbert-Fedorov shifts of polarized vortex beams. Optics Letters, 2009, 34(3): 389–391
18. Kong L J, Wang X L, Li S M, Li Y N, Chen J, Gu B, Wang H T. Spin Hall effect of reflected light from an air-glass interface around the Brewster's angle. Applied Physics Letters, 2012, 100(7): 071109
19. Kapitanova P V, Ginzburg P, Rodríguez-Fortuño F J, Filonov D S, Voroshilov P M, Belov P A, Poddubny A N, Kivshar Y S, Wurtz G A, Zayats A V. Photonic spin Hall effect in hyperbolic metamaterials for polarization-controlled routing of subwavelength modes. Nature Communications, 2014, 5: 3226
20. Zhang Y, Li P, Liu S, Han L, Cheng H C, Zhao J L. Optimized weak measurement for spatial spin-dependent shifts at Brewster angle. Applied Physics B, Lasers and Optics, 2016, 122(7): 184
21. Bliokh K Y. Geometrical optics of beams with vortices: Berry phase and orbital angular momentum Hall effect. Physical Review Letters, 2006, 97(4): 043901
22. Merano M, Hermosa N, Woerdman J P, Aiello A. How orbital angular momentum affects beam shifts in optical reflection. Physical Review A, Atomic, Molecular, and Optical Physics, 2010, 82(2): 023817
23. Dooghin A V, Kundikova N D, Liberman V S, Zel'dovich B Y. Optical Magnus effect. Physical Review A, Atomic, Molecular, and Optical Physics, 1992, 45(11): 8204–8208
24. Van Enk S J, Nienhuis G. Spin and orbital angular momentum of photons. Europhysics Letters, 1994, 25(7): 497–501
25. Yao A M, Padgett M J. Orbital angular momentum: origins, behavior and applications. Advances in Optics and Photonics,

2011, 3(2): 161–204
26. Allen L, Padgett M J. The Poynting vector in Laguerre–Gaussian beams and the interpretation of their angular momentum density. Optics Communications, 2000, 184(1–4): 67–71
27. Barnett S M, Allen L. Orbital angular momentum and nonparaxial light beams. Optics Communications, 1994, 110(5–6): 670–678
28. Babiker M, Power W L, Allen L. Light-induced torque on moving atoms. Physical Review Letters, 1994, 73(9): 1239–1242
29. Simpson N B, Dholakia K, Allen L, Padgett M J. Mechanical equivalence of spin and orbital angular momentum of light: an optical spanner. Optics Letters, 1997, 22(1): 52–54
30. Grier D G. A revolution in optical manipulation. Nature, 2003, 424 (6950): 810–816
31. Padgett M, Allen L. Optical tweezers and spanners. Physics World, 1997, 10(9): 35–40
32. Bowman R W, Padgett M J. Optical trapping and binding. Reports on Progress in Physics, 2013, 76(2): 026401
33. Bozinovic N, Yue Y, Ren Y, Tur M, Kristensen P, Huang H, Willner A E, Ramachandran S. Terabit-scale orbital angular momentum mode division multiplexing in fibers. Science, 2013, 340(6140): 1545–1548
34. Zhang Y, Djordjevic I B, Gao X. On the quantum-channel capacity for orbital angular momentum-based free-space optical communications. Optics Letters, 2012, 37(15): 3267–3269
35. Leach J, Jack B, Romero J, Jha A K, Yao A M, Franke-Arnold S, Ireland D G, Boyd R W, Barnett S M, Padgett M J. Quantum correlations in optical angle-orbital angular momentum variables. Science, 2010, 329(5992): 662–665
36. Wang J. Advances in communications using optical vortices. Photonics Research, 2016, 4(5): B14–B28
37. Malik M, Mirhosseini M, Lavery M P J, Leach J, Padgett M J, Boyd R W. Direct measurement of a 27-dimensional orbital-angular-momentum state vector. Nature Communications, 2014, 5: 3115
38. Su T, Scott R P, Djordjevic S S, Fontaine N K, Geisler D J, Cai X, Yoo S J B. Demonstration of free space coherent optical communication using integrated silicon photonic orbital angular momentum devices. Optics Express, 2012, 20(9): 9396–9402
39. Yan Y, Yue Y, Huang H, Yang J Y, Chitgarha M R, Ahmed N, Tur M, Dolinar S J, Willner A E. Efficient generation and multiplexing of optical orbital angular momentum modes in a ring fiber by using multiple coherent inputs. Optics Letters, 2012, 37(17): 3645–3647
40. Wang J, Yang J Y, Fazal I M, Ahmed N, Yan Y, Huang H, Ren Y X, Yue Y, Dolinar S, Tur M, Willner A E. Terabit free-space data transmission employing orbital angular momentum multiplexing. Nature Photonics, 2012, 6(7): 488–496
41. Willner A E, Huang H, Yan Y, Ren Y, Ahmed N, Xie G, Bao C, Li L, Cao Y, Zhao Z, Wang J, Lavery M P J, Tur M, Ramachandran S, Molisch A F, Ashrafi N, Ashrafi S. Optical communications using orbital angular momentum beams. Advances in Optics and Photonics, 2015, 7(1): 66–106
42. Mair A, Vaziri A, Weihs G, Zeilinger A. Entanglement of the orbital angular momentum states of photons. Nature, 2001, 412 (6844): 313–316
43. Oemrawsingh S S, Ma X, Voigt D, Aiello A, Eliel E R, 't Hooft G W, Woerdman J P. Experimental demonstration of fractional orbital angular momentum entanglement of two photons. Physical Review Letters, 2005, 95(24): 240501
44. Karimi E, Marrucci L, de Lisio C, Santamato E. Time-division multiplexing of the orbital angular momentum of light. Optics Letters, 2012, 37(2): 127–129
45. Müller M, Bounouar S, Jöns K D, Glässl M, Michler P. On-demand generation of indistinguishable polarization-entangled photon pairs. Nature Photonics, 2014, 8(3): 224–228
46. Wang X L, Cai X D, Su Z E, Chen M C, Wu D, Li L, Liu N L, Lu C Y, Pan J W. Quantum teleportation of multiple degrees of freedom of a single photon. Nature, 2015, 518(7540): 516–519
47. Lavery M P J, Speirits F C, Barnett S M, Padgett M J. Detection of a spinning object using light's orbital angular momentum. Science, 2013, 341(6145): 537–540
48. Löffler W, Aiello A, Woerdman J P. Observation of orbital angular momentum sidebands due to optical reflection. Physical Review Letters, 2012, 109(11): 113602
49. Chen R P, Chen Z, Chew K H, Li P G, Yu Z, Ding J, He S. Structured caustic vector vortex optical field: manipulating optical angular momentum flux and polarization rotation. Scientific Reports, 2015, 5(1): 10628
50. Pan Y, Gao X Z, Ren Z C, Wang X L, Tu C, Li Y, Wang H T. Arbitrarily tunable orbital angular momentum of photons. Scientific Reports, 2016, 6(1): 29212
51. Beijersbergen M W, Allen L, Van der Veen H, Woerdman J P. Astigmatic laser mode converters and transfer of orbital angular momentum. Optics Communications, 1993, 96(1-3): 123–132
52. Indebetouw G. Optical vortices and their propagation. Journal of Modern Optics, 1993, 40(1): 73–87
53. Roux F S. Dynamical behavior of optical vortices. Journal of the Optical Society of America B, Optical Physics, 1995, 12(7): 1215–1221
54. Zhao X Y, Zhang J C, Pang X Y, Wan G B. Properties of a strongly focused Gaussian beam with an off-axis vortex. Optics Communications, 2017, 389: 275–282
55. Rozas D, Law C T, Swartzlander G A Jr. Propagation dynamics of optical vortices. Journal of the Optical Society of America B, Optical Physics, 1997, 14(11): 3054–3065
56. Gan X T, Zhao J L, Liu S, Fang L. Generation and motion control of optical multi-vortex. Chinese Optics Letters, 2009, 7(12): 1142–1145
57. Peng Y, Gan X T, Ju P, Wang Y D, Zhao J L. Measuring topological charges of optical vortices with multi-singularity using a cylindrical lens. Chinese Physics Letters, 2015, 32(2): 024201
58. Padgett M J, Miatto F M, Lavery M P J, Zeilinger A, Boyd R W. Divergence of an orbital-angular-momentum-carrying beam upon propagation. New Journal of Physics, 2015, 17(2): 023011
59. Porras M A, Borghi R, Santarsiero M. Relationship between elegant Laguerre-Gauss and Bessel-Gauss beams. Journal of the Optical Society of America A, Optics, Image Science, and Vision, 2001, 18(1): 177–184
60. Mendoza-Hernández J, Arroyo-Carrasco M L, Iturbe-Castillo M D, Chávez-Cerda S. Laguerre-Gauss beams versus Bessel beams showdown: peer comparison. Optics Letters, 2015, 40(16): 3739–3742
61. Bencheikh A, Fromager M, Ameur K A. Generation of Laguerre-

Gaussian LG_{p0} beams using binary phase diffractive optical elements. Applied Optics, 2014, 53(21): 4761–4767
62. Haddadi S, Louhibi D, Hasnaoui A, Harfouche A, Aït-Ameur K. Spatial properties of a diffracted high-order radial Laguerre–Gauss LG_{p0} beam. Laser Physics, 2015, 25(12): 125002
63. Li L, Xie G D, Yan Y, Ren Y X, Liao P C, Zhao Z, Ahmed N, Wang Z, Bao C J, Willner A J, Ashrafi S, Tur M, Willner A E. Power loss mitigation of orbital-angular-momentum-multiplexed free-space optical links using nonzero radial index Laguerre–Gaussian beams. Journal of the Optical Society of America B, Optical Physics, 2017, 34(1): 1–6
64. Hamazaki J, Mineta Y, Oka K, Morita R. Direct observation of Gouy phase shift in a propagating optical vortex. Optics Express, 2006, 14(18): 8382–8392
65. Amaral A M, Falcão-Filho E L, de Araújo C B. Shaping optical beams with topological charge. Optics Letters, 2013, 38(9): 1579–1581
66. Hermosa N P II, Manaois C O. Phase structure of helico-conical optical beams. Optics Communications, 2007, 271(1): 178–183
67. Alonzo C, Rodrigo P J, Glückstad J. Helico-conical optical beams: a product of helical and conical phase fronts. Optics Express, 2005, 13(5): 1749–1760
68. Daria V R, Palima D Z, Glückstad J. Optical twists in phase and amplitude. Optics Express, 2011, 19(2): 476–481
69. Götte J B, O'Holleran K, Preece D, Flossmann F, Franke-Arnold S, Barnett S M, Padgett M J. Light beams with fractional orbital angular momentum and their vortex structure. Optics Express, 2008, 16(2): 993–1006
70. Nugrowati A M, Stam W G, Woerdman J P. Position measurement of non-integer OAM beams with structurally invariant propagation. Optics Express, 2012, 20(25): 27429–27441
71. Maji S, Brundavanam M M. Controlled noncanonical vortices from higher-order fractional screw dislocations. Optics Letters, 2017, 42(12): 2322–2325
72. Dai H T, Liu Y J, Luo D, Sun X W. Propagation properties of an optical vortex carried by an Airy beam: experimental implementation. Optics Letters, 2011, 36(9): 1617–1619
73. Chu X. Propagation of an Airy beam with a spiral phase. Optics Letters, 2012, 37(24): 5202–5204
74. Rosales-Guzmán C, Mazilu M, Baumgartl J, Rodríguez-Fajardo V, Ramos-García R, Dholakia K. Collision of propagating vortices embedded within Airy beams. Journal of Optics, 2013, 15(4): 044001
75. Kim G H, Lee H J, Kim L U, Suk H. Propagation dynamics of optical vortices with anisotropic phase profiles. Journal of the Optical Society of America B, Optical Physics, 2003, 20(2): 351–359
76. Curtis J E, Grier D G. Modulated optical vortices. Optics Letters, 2003, 28(11): 872–874
77. Rodrigo J A, Alieva T, Abramochkin E, Castro I. Shaping of light beams along curves in three dimensions. Optics Express, 2013, 21 (18): 20544–20555
78. Rodrigo J A, Alieva T. Freestyle 3D laser traps: tools for studying light-driven particle dynamics and beyond. Optica, 2015, 2(9): 812–815
79. Li P, Liu S, Peng T, Xie G, Gan X, Zhao J. Spiral autofocusing Airy beams carrying power-exponent-phase vortices. Optics Express, 2014, 22(7): 7598–7606
80. Chremmos I, Efremidis N K, Christodoulides D N. Pre-engineered abruptly autofocusing beams. Optics Letters, 2011, 36(10): 1890–1892
81. Papazoglou D G, Efremidis N K, Christodoulides D N, Tzortzakis S. Observation of abruptly autofocusing waves. Optics Letters, 2011, 36(10): 1842–1844
82. Jiang Y, Huang K, Lu X. Propagation dynamics of abruptly autofocusing Airy beams with optical vortices. Optics Express, 2012, 20(17): 18579–18584
83. Chen B, Chen C, Peng X, Peng Y, Zhou M, Deng D. Propagation of sharply autofocused ring Airy Gaussian vortex beams. Optics Express, 2015, 23(15): 19288–19298
84. Zhang Y, Li P, Liu S, Han L, Cheng H, Zhao J. Manipulating spin-dependent splitting of vector abruptly autofocusing beam by encoding cosine-azimuthal variant phases. Optics Express, 2016, 24(25): 28409–28418
85. Wang F, Zhao C L, Dong Y, Dong Y M, Cai Y J. Generation and tight-focusing properties of cylindrical vector circular Airy beams. Applied Physics B, Lasers and Optics, 2014, 117(3): 905–913
86. Wang X L, Ding J, Ni W J, Guo C S, Wang H T. Generation of arbitrary vector beams with a spatial light modulator and a common path interferometric arrangement. Optics Letters, 2007, 32(24): 3549–3551
87. Wang X L, Chen J, Li Y, Ding J, Guo C S, Wang H T. Optical orbital angular momentum from the curl of polarization. Physical Review Letters, 2010, 105(25): 253602
88. Liu S, Li P, Peng T, Zhao J. Generation of arbitrary spatially variant polarization beams with a trapezoid Sagnac interferometer. Optics Express, 2012, 20(19): 21715–21721
89. Marrucci L, Manzo C, Paparo D. Optical spin-to-orbital angular momentum conversion in inhomogeneous anisotropic media. Physical Review Letters, 2006, 96(16): 163905
90. Biener G, Niv A, Kleiner V, Hasman E. Formation of helical beams by use of Pancharatnam-Berry phase optical elements. Optics Letters, 2002, 27(21): 1875–1877
91. Yu N, Genevet P, Kats M A, Aieta F, Tetienne J P, Capasso F, Gaburro Z. Light propagation with phase discontinuities: generalized laws of reflection and refraction. Science, 2011, 334(6054): 333–337
92. Yu N, Capasso F. Flat optics with designer metasurfaces. Nature Materials, 2014, 13(2): 139–150
93. Zhang L, Mei S T, Huang K, Qiu C W. Advances in full control of electromagnetic waves with metasurfaces. Advanced Optical Materials, 2016, 4(6): 818–833
94. Estakhri N M, Alù A. Recent progress in gradient metasurfaces. Journal of the Optical Society of America B, Optical Physics, 2016, 33(2): A21–A30
95. Epstein A, Eleftheriades G V. Huygens' metasurfaces via the equivalence principle: design and applications. Journal of the Optical Society of America B, Optical Physics, 2016, 33(2): A31–A50
96. Marrucci L, Karimi E, Slussarenko S, Piccirillo B, Santamato E, Nagali E, Sciarrino F. Spin-to-orbital conversion of the angular momentum of light and its classical and quantum applications.

Journal of Optics, 2011, 13(6): 064001
97. Cardano F, Marrucci L. Spin-orbit photonics. Nature Photonics, 2015, 9(12): 776–778
98. Berry M V. The adiabatic phase and Pancharatnam phase for polarized light. Journal of Modern Optics, 1987, 34(11): 1401–1407
99. Liu S, Li P, Zhang Y, Gan X, Wang M, Zhao J. Longitudinal spin separation of light and its performance in three-dimensionally controllable spin-dependent focal shift. Scientific Reports, 2016, 6 (1): 20774
100. Milione G, Sztul H I, Nolan D A, Alfano R R. Higher-order Poincaré sphere, stokes parameters, and the angular momentum of light. Physical Review Letters, 2011, 107(5): 053601
101. Wang X L, Li Y, Chen J, Guo C S, Ding J, Wang H T. A new type of vector fields with hybrid states of polarization. Optics Express, 2010, 18(10): 10786–10795
102. Yi X N, Liu Y C, Ling X H, Zhou X X, Ke Y G, Luo H L, Wen S C, Fan D Y. Hybrid-order Poincaré sphere. Physical Review A, Atomic, molecular, and optical physics, 2015, 91: 023801
103. Ren Z C, Kong L J, Li S M, Qian S X, Li Y, Tu C, Wang H T. Generalized Poincaré sphere. Optics Express, 2015, 23(20): 26586–26595
104. Gorodetski Y, Biener G, Niv A, Kleiner V, Hasman E. Space-variant polarization manipulation for far-field polarimetry by use of subwavelength dielectric gratings. Optics Letters, 2005, 30(17): 2245–2247
105. Niv A, Biener G, Kleiner V, Hasman E. Rotating vectorial vortices produced by space-variant subwavelength gratings. Optics Letters, 2005, 30(21): 2933–2935
106. Biener G, Gorodetski Y, Niv A, Kleiner V, Hasman E. Manipulation of polarization-dependent multivortices with quasi-periodic subwavelength structures. Optics Letters, 2006, 31(11): 1594–1596
107. Shitrit N, Yulevich I, Maguid E, Ozeri D, Veksler D, Kleiner V, Hasman E. Spin-optical metamaterial route to spin-controlled photonics. Science, 2013, 340(6133): 724–726
108. Yin X, Ye Z, Rho J, Wang Y, Zhang X. Photonic spin Hall effect at metasurfaces. Science, 2013, 339(6126): 1405–1407
109. Slussarenko S, Alberucci A, Jisha C P, Piccirillo B, Santamato E, Assanto G, Marrucci L. Guiding light via geometric phases. Nature Photonics, 2016, 10(9): 571–575
110. Philip G M, Kumar V, Milione G, Viswanathan N K. Manifestation of the Gouy phase in vector-vortex beams. Optics Letters, 2012, 37 (13): 2667–2669
111. Niv A, Biener G, Kleiner V, Hasman E. Manipulation of the Pancharatnam phase in vectorial vortices. Optics Express, 2006, 14 (10): 4208–4220
112. Shu W X, Ke Y G, Liu Y C, Ling X H, Luo H L, Yin X B. Radial spin Hall effect of light. Physical Review A, Atomic, molecular, and optical physics, 2016, 93(1): 013839
113. Li P, Zhang Y, Liu S, Ma C, Han L, Cheng H, Zhao J. Generation of perfect vectorial vortex beams. Optics Letters, 2016, 41(10): 2205–2208
114. Zhang W, Liu S, Li P, Jiao X, Zhao J. Controlling the polarization singularities of the focused azimuthally polarized beams. Optics Express, 2013, 21(1): 974–983
115. Baumann S M, Kalb D M, MacMillan L H, Galvez E J. Propagation dynamics of optical vortices due to Gouy phase. Optics Express, 2009, 17(12): 9818–9827
116. Liu S, Wang M, Li P, Zhang P, Zhao J. Abrupt polarization transition of vector autofocusing Airy beams. Optics Letters, 2013, 38(14): 2416–2418
117. Bomzon Z, Niv A, Biener G, Kleiner V, Hasman E. Nondiffracting periodically space-variant polarization beams with subwavelength gratings. Applied Physics Letters, 2002, 80(20): 3685–3687
118. Bomzon Z, Biener G, Kleiner V, Hasman E. Space-variant Pancharatnam-Berry phase optical elements with computer-generated subwavelength gratings. Optics Letters, 2002, 27(13): 1141–1143
119. Ling X H, Zhou X X, Yi X N, Shu W X, Liu Y C, Chen S Z, Luo H L, Wen S C, Fan D Y. Giant photonic spin Hall effect in momentum space in a structured metamaterial with spatially varying birefringence. Light, Science & Applications, 2015, 4(5): e290
120. Ke Y G, Liu Y C, He Y L, Zhou J X, Luo H L, Wen S C. Realization of spin-dependent splitting with arbitrary intensity patterns based on all-dielectric metasurfaces. Applied Physics Letters, 2015, 107(4): 041107
121. Gorodetski Y, Biener G, Niv A, Kleiner V, Hasman E. Optical properties of polarization-dependent geometric phase elements with partially polarized light. Optics Communications, 2006, 266 (2): 365–375
122. Ke Y G, Liu Y C, Zhou J X, Liu Y Y, Luo H L, Wen S C. Optical integration of Pancharatnam-Berry phase lens and dynamical phase lens. Applied Physics Letters, 2016, 108(10): 101102
123. Hasman E, Kleiner V, Biener G, Niv A. Polarization dependent focusing lens by use of quantized Pancharatnam–Berry phase diffractive optics. Applied Physics Letters, 2003, 82(3): 328–330
124. Ni X J, Ishii S, Kildishev A V, Shalaev V M. Ultra-thin, planar, Babinet-inverted plasmonic metalenses. Light, Science & Applications, 2013, 2(4): e72
125. Gao K, Cheng H H, Bhowmik A K, Bos P J. Thin-film Pancharatnam lens with low f-number and high quality. Optics Express, 2015, 23(20): 26086–26094
126. Ding X, Monticone F, Zhang K, Zhang L, Gao D, Burokur S N, de Lustrac A, Wu Q, Qiu C W, Alù A. Ultrathin pancharatnam-berry metasurface with maximal cross-polarization efficiency. Advanced Materials, 2015, 27(7): 1195–1200
127. Chen X Z, Chen M, Mehmood M Q, Wen D D, Yue F Y, Qiu C W, Zhang S. Longitudinal multifoci metalens for circularly polarized light. Advanced Optical Matericals, 2015, 3(9): 1201–1206
128. Li X, Lan T H, Tien C H, Gu M. Three-dimensional orientation-unlimited polarization encryption by a single optically configured vectorial beam. Nature Communications, 2012, 3: 998
129. Zheng G, Mühlenbernd H, Kenney M, Li G, Zentgraf T, Zhang S. Metasurface holograms reaching 80% efficiency. Nature Nanotechnology, 2015, 10(4): 308–312
130. Cardano F, Karimi E, Marrucci L, de Lisio C, Santamato E. Generation and dynamics of optical beams with polarization singularities. Optics Express, 2013, 21(7): 8815–8820
131. Moreno I, Davis J A, Sánchez-López M M, Badham K, Cottrell D M. Nondiffracting Bessel beams with polarization state that varies

with propagation distance. Optics Letters, 2015, 40(23): 5451–5454
132. Davis J A, Moreno I, Badham K, Sánchez-López M M, Cottrell D M. Nondiffracting vector beams where the charge and the polarization state vary with propagation distance. Optics Letters, 2016, 41(10): 2270–2273
133. Li P, Zhang Y, Liu S, Cheng H, Han L, Wu D, Zhao J. Generation and self-healing of vector Bessel-Gauss beams with variant state of polarizations upon propagation. Optics Express, 2017, 25(5): 5821–5831
134. Gao X Z, Pan Y, Li S M, Wang D, Li Y N, Tu C H, Wang H T. Vector optical fields broken in the spatial frequency domain. Physical Review A, Atomic, molecular, and optical physics, 2016, 93(3): 033834
135. Davis J A, Bentley J B. Azimuthal prism effect with partially blocked vortex-producing lenses. Optics Letters, 2005, 30(23): 3204–3206
136. Vyas S, Kozawa Y, Sato S. Self-healing of tightly focused scalar and vector Bessel-Gauss beams at the focal plane. Journal of the Optical Society of America A, Optics, Image Science, and Vision, 2011, 28(5): 837–843
137. Vyas S, Niwa M, Kozawa Y, Sato S. Diffractive properties of obstructed vector Laguerre-Gaussian beam under tight focusing condition. Journal of the Optical Society of America A, Optics, Image Science, and Vision, 2011, 28(7): 1387–1394
138. Wang X L, Lou K, Chen J, Gu B, Li Y N, Wang H T. Unveiling locally linearly polarized vector fields with broken axial symmetry. Physical Review A, Atomic, molecular, and optical physics, 2011, 83(6): 063813
139. Jiao X, Liu S, Wang Q, Gan X, Li P, Zhao J. Redistributing energy flow and polarization of a focused azimuthally polarized beam with rotationally symmetric sector-shaped obstacles. Optics Letters, 2012, 37(6): 1041–1043
140. Wu G F, Wang F, Cai Y J. Generation and self-healing of a radially polarized Bessel-Gauss beam. Physical Review A, Atomic, molecular, and optical physics, 2014, 89(4): 043807
141. Franke-Arnold S, Barnett S M, Yao E, Leach J, Courtial J, Padgett M. Uncertainty principle for angular position and angular momentum. New Journal of Physics, 2004, 6: 103
142. Yao E, Franke-Arnold S, Courtial J, Barnett S, Padgett M. Fourier relationship between angular position and optical orbital angular momentum. Optics Express, 2006, 14(20): 9071–9076
143. Jack B, Padgett M J, Franke-Arnold S. Angular diffraction. New Journal of Physics, 2008, 10(10): 103013
144. Li P, Liu S, Xie G, Peng T, Zhao J. Modulation mechanism of multi-azimuthal masks on the redistributions of focused azimuthally polarized beams. Optics Express, 2015, 23(6): 7131–7139
145. Zhang Y, Li P, Liu S, Zhao J. Unveiling the photonic spin Hall effect of freely propagating fan-shaped cylindrical vector vortex beams. Optics Letters, 2015, 40(19): 4444–4447
146. Cai Y J, Lü X. Propagation of Bessel and Bessel–Gaussian beams through an unapertured or apertured misaligned paraxial optical systems. Optics Communications, 2007, 274(1): 1–7
147. Liu X L, Peng X F, Liu L, Wu G F, Zhao C L, Wang F, Cai Y J. Self-reconstruction of the degree of coherence of a partially coherent vortex beam obstructed by an opaque obstacle. Applied Physics Letters, 2017, 110(18): 181104
148. Ling X H, Yi X N, Zhou X X, Liu Y C, Shu W X, Luo H L, Wen S C. Realization of tunable spin-dependent splitting in intrinsic photonic spin Hall effect. Applied Physics Letters, 2014, 105(15): 151101
149. Li P, Liu S, Zhang Y, Xie G F, Zhao J L. Experimental realization of focal field engineering of the azimuthally polarized beams modulated by multi-azimuthal masks. Journal of the Optical Society of America B, Optical Physics, 2015, 32(9): 1867–1872

Peng Li is currently an Associate Professor at the School of Science, Northwestern Polytechnical University (NPU), Xi'an, China. He received the Ph.D. degree in Optical Engineering from the Department of Applied Physics at NPU in 2013. His research interests include structured optical fields, nanophotonics, and multi-core fibers. He has published more than 30 technical papers in optics related fields.

Sheng Liu received the Ph.D. degree in Optical Engineering from the Department of Applied Physics at Northwestern Polytechnical University (NPU) of China in 2011. He is currently an Associate Professor at the School of Science, NPU, Xi'an, China. His research interests include generation and modulation of optical fields, photonic lattices, and spatial solitons. He has published more than 50 technical papers in optics related fields.

Yi Zhang received the B.S. degree in Optical Information Science and Technology from the Department of Applied Physics at Northwestern Polytechnical University (NPU) of China in 2013. He is currently a Ph.D. student in Optical Engineering at the School of Science, NPU, China. His research interests include complex light fields, optical spin-orbital interaction. He has published 13 technical papers in optics related fields.

Lei Han received the B.S. degree in Optical Information Science and Technology from the Department of Applied Physics at Northwestern Polytechnical University (NPU) of China in 2014. He is currently a Ph.D. student in Optical Engineering at the School of Science, NPU, China. His research work focuses on the focusing properties of spatial structured light fields and its applications. Now he is visiting the

National University of Singapore as a joint Ph.D. student funded by China Scholarship Council.

Dongjing Wu received the B.S. degree in Optical Information Science and Technology from the Department of Applied Physics at Northwestern Polytechnical University (NPU) of China in 2016. He is currently working toward the M.S. degree in Optical Engineering in NPU, China. His research work focuses on the construction of spatial structured light fields with longitudinally varying polarization.

Huachao Cheng received the B.S. degree in Optical Information Science and Technology from the Department of Applied Physics at Northwestern Polytechnical University (NPU) of China in 2015. He is now a Ph.D. student at the School of Science, NPU, China. His research interests are mainly in exploring the interaction between structured femtosecond pulses and materials.

Shuxia Qi received the B.S. degree in Applied Physics from Northeastern University of China in 2016. She is currently a master student at the School of Science, Northwestern Polytechnical University, China. Her research interests are mainly in constructing complex light fields, efficiently generating vector beams and exploring its spatial evolution.

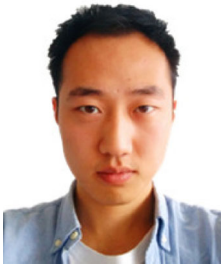

Xuyue Guo received the B.S. degree in Optical Information Science and Technology from the Department of Applied Physics at Northwestern Polytechnical University (NPU) of China in 2017. He is currently a Ph.D. student at the School of Science, NPU, China. His research interests are mainly in exploring the focusing properties of vector beams and multifocal array.

Jianlin Zhao is now a Professor at the School of Science, Northwestern Polytechnical University, Xi'an, China. Prof. Zhao received his Ph.D. degree in Optics from the Xi'an Institute of Optics and Precision Mechanics, Chinese Academy of Sciences, in 1998. Prof. Zhao is also the director of the Shaanxi Key Laboratory of Optical Information Technology and the MOE Key Laboratory of Material Physics and Chemistry under Extraordinary Conditions. He has published over 480 journal and international conference papers in the fields of digital holography, light field control and information processing, nonlinear optics, micro-nano photonics and optical fiber sensors.